



Efficient promotion of ethanol complete electrooxidation by anti-poisoning rhodium-bismuth alloy nanodendrites

Bo-Qiang Miao^a, Bin Sun^a, Tian-Jiao Wang^a, Feng Shi^a, Pei Chen^a, Pu-Jun Jin^a, Dong-Sheng Li^b, Fu-Min Li^{c,*}, Yu Chen^{a,*}

^a Key Laboratory of Macromolecular Science of Shaanxi Province, Key Laboratory of Applied Surface and Colloid Chemistry (Ministry of Education), Shaanxi Key Laboratory for Advanced Energy Devices, School of Materials Science and Engineering, Shaanxi Normal University, Xi'an 710062, PR China

^b College of Materials and Chemical Engineering, Key Laboratory of Inorganic Nonmetallic Crystalline and Energy Conversion Materials, China Three Gorges University, Yichang 443002, PR China

^c School of Chemistry and Chemical Engineering, Huazhong University of Science and Technology, Wuhan 430074, PR China

ARTICLE INFO

Keywords:

Alkaline direct ethanol fuel cells
RhBi alloy nanodendrites
Ethanol oxidation reaction
C1 pathway
Anti-poisoning ability

ABSTRACT

Alkaline direct ethanol fuel cells are promising future energy technologies with a high energy-density, while the lack of robust anodic electrocatalysts limits their energy conversion efficiency due to serious poisoning and weak selectivity to the C1 pathway of ethanol oxidation reaction (EOR). Herein, rhodium-bismuth alloy nanodendrites (RhBi-NDs) are applied as an efficient and anti-poisoning electrocatalyst for EOR, which exhibit superior electrocatalytic performance, including a mass activity of 1068.9 mA mg_{Rh}⁻¹ at 0.71 V, a 31.1% Faradaic efficiency for the C1 product, and an excellent stability of 40 h. The mechanism study indicates that Bi improves the oxidation ability of Rh to toxic intermediates by providing oxygen-containing species. The theoretical calculations disclose the electronic interaction between Bi and Rh, which tunes the adsorption energy of intermediates such as CH₃CH₂OH*, and CH₃CO*, resulting in the suppression of C2 pathway and the promotion of C1 pathway for EOR on RhBi-NDs.

1. Introduction

Fuel cells are advanced energy conversion apparatus that convert chemical energy into electrical energy, with the advantages of high energy conversion efficiency and green environmental protection [1–8]. Direct ethanol fuel cells are fast-developing liquid fuel cells in recent years, which have a simple structure, easy miniaturization, safe operation, fast start-up at low temperature, and excellent potential for portable power applications. Furthermore, the fuel ethanol used in direct ethanol fuel cells is abundant, renewable, easy to store and transport, non-toxic, and has high energy density [9–11]. Alkaline direct ethanol fuel cells (ADEFCs) operating in alkaline media have significant advantages with respect to acidic direct ethanol fuel cells. First, the ethanol oxidation reaction (EOR) in alkaline media has smaller overpotential and faster reaction kinetics than that in acid media, which can increase the power density and open circuit voltage of ADEFCs [12–16]. Secondly, advanced electrocatalysts based on non-precious metal materials can be utilized for cathode oxygen reduction reaction in alkaline media, which can effectively reduce the cost of ADEFCs [17–21].

At present, the bottleneck of ADEFCs is the slow kinetics of EOR and the incomplete oxidation of ethanol. Ideally, the anodic EOR process begins with the initial dehydrogenation of ethanol molecule to produce reaction intermediates (such as CH₃CO_{ad}) [22,23]. Subsequently, the carbon-carbon (C-C) bond of these intermediates is cleaved, forming CH_x or CO_{ad}, which can be further dehydrogenated to form C1 product (i.e., CO₂) and water. This so-called C1 pathway can release up to 12 electrons. However, the most commonly used platinum (Pt) and palladium (Pd) electrocatalysts are not effective for breaking the C-C bond of ethanol [24–27]. Although lower EOR potentials and higher oxidation current densities can be obtained by constructing Pt/Pd-based alloy nanomaterials, these electrocatalysts are still inefficient in breaking C-C bonds. Concurrently, the easily poisoned nature of Pt and Pd makes it difficult to guarantee the EOR stability. Therefore, efficient and anti-poisoning EOR electrocatalysts are still scarce for practical ADEFCs. Recently, Rh-based nanomaterials as alkaline EOR electrocatalysts have been studied [28–30]. Both experiments and theoretical calculations have confirmed that Rh is more effective than Pt and Pd in breaking C-C bonds for alkaline EOR, and Rh inherently possesses better

* Corresponding authors.

E-mail addresses: lifuminxs@gmail.com (F.-M. Li), ndchenyu@gmail.com (Y. Chen).

<https://doi.org/10.1016/j.apcatb.2023.122967>

Received 13 March 2023; Received in revised form 1 June 2023; Accepted 5 June 2023

Available online 7 June 2023

0926-3373/© 2023 Elsevier B.V. All rights reserved.

anti-poisoning ability than Pt and Pd [31,32]. In addition, the EOR performance of Rh-based nanomaterials can be further improved by combining morphology optimization and component modulation strategies [33–37]. For example, Huang's group reported that two-dimensional ultrathin Rh-SnO₂ nanosheets showed significantly enhanced EOR performance with a selectivity of up to 77.1% for C1 product [38]. The analysis indicates that the bifunctional mechanism triggered by the Rh-SnO₂ interface facilitates the generation of C1 products, as the highly oxygenophilic SnO₂ provides abundant interfacial oxygen species (OH_{ad}) that promote the oxidation of adsorbed poisonous species, such as CH_x and CO. However, the EOR mass activity of Rh-based nanomaterials still cannot meet commercial requirements and needs further improvement.

Herein, we report the synthesis of Rh-Bismuth alloys nanodendrites (RhBi-NDs) with high EOR performance. On the one hand, the three-dimensional nanodendrites with open structures usually show better electrocatalytic activity relative to conventional solid nanospheres due to their high porosity and abundant active atoms. On the other hand, Rh-Bi cooperation, including electronic effect and bifunctional mechanism, achieves promoted C1 pathway, excellent anti-poisoning ability, and higher EOR mass activity than commercial Rh, Pt, and Pd catalysts. Especially, the Faradaic efficiency for the C1 pathway of EOR on RhBi-NDs reaches to 31.1%, which was significantly higher than that on commercial Rh, Pt, and Pd catalysts.

2. Results and discussion

2.1. Physical characterization of Rh₇Bi₁-NDs

RhBi-NDs were prepared by using the solvothermal method. The elemental content of Rh₇Bi₁-NDs was analyzed using energy-dispersive X-ray spectroscopy (EDX) patterns. The experimental data reveal that the Rh/Bi atomic ratio is approximately 87.3/12.7 (Fig. 1a), which is close to the sample feeding ratio of 7/1 (defined as Rh₇Bi₁-NDs) and the test result of inductively coupled plasma atomic emission spectroscopy (ICP-AES). The phase structure of Rh₇Bi₁-NDs was analyzed by X-ray diffraction (XRD) measurements. Herein, all diffraction peaks of Rh₇Bi₁-NDs slightly deviated from the standard PDF card of Rh metal (PDF No.

05–0685) towards a small angle, indicating that Rh₇Bi₁-NDs is a Rh-Bi alloy (Fig. 1b). Concurrently, the Bi content is calculated to be 12.10% based on Vegard's law, indicating a high alloy degree of Rh₇Bi₁-NDs. To further investigate the surface composition of Rh₇Bi₁-NDs, surface analysis was carried out by using X-ray photoelectron spectrometer (XPS). The deconvoluted XPS fine spectrum of the Rh 3d orbit is divided into two groups of peaks, and the peaks at 306.86/311.60 eV and 308.06/312.76 eV indicate the presence of Rh⁰ and Rh³⁺ species, respectively (Fig. 1c). Concurrently, the corresponding peak areas of Rh⁰ and Rh³⁺ species are 81% and 19%, respectively, indicating partial oxidation occurs on the Rh₇Bi₁-NDs surface due to air oxidation [39]. Further observation shows that the binding energy of Rh⁰ on the Rh₇Bi₁-NDs surface is slightly shifted with respect to the standard binding energy of metallic Rh, which is due to difference in electronegativity between Rh and Bi [40]. The 4f orbital fine spectrum of Bi signal shows that Bi signal is also fitted by splitting into Bi⁰ and Bi³⁺ (Fig. 1d). The appearance of the Bi⁰ specie indicates that the Bi salt is successfully reduced in the synthesis process. Since nanostructured Bi is easily oxidized by oxygen in air, the proportion of Bi³⁺ specie revealed by XPS is significantly higher than that of Bi⁰ specie [41]. Moreover, the binding energy of Bi⁰ shifts positively, confirming the electrons transfer from Bi to Rh in Rh₇Bi₁-NDs.

The morphology of Rh₇Bi₁-NDs was characterized by transmission electron microscopy (TEM). A classical nanodendrite structure with a rough surface and good dispersibility is revealed (Fig. 2a). The particle size distribution plot displays that the mean particle size of Rh₇Bi₁-NDs is 16.3 nm (Fig. S1). The width of each subunit nanobranch can be determined to be only about 4 nm (Fig. 2b). The smaller the particle size means the more active sites, indicating that Rh₇Bi₁-NDs have a promising application in catalysis. The high-resolution transmission electron microscopy (HRTEM) image shows rich pores and channels on the surface of Rh₇Bi₁-NDs (Fig. 2c). The corresponding selected area electron diffraction (SAED) pattern of Rh₇Bi₁-NDs exhibit the typical polycrystalline diffraction ring shape, and all diffraction rings can correspond to specific crystal planes of the RhBi alloy. Furthermore, the distinct lattice stripes with lattice spacings of 0.227 and 0.198 nm can be observed on the HR-TEM image, which are slightly larger than the (111) and (200) plane spacings of Rh with face centered cubic phase structure,

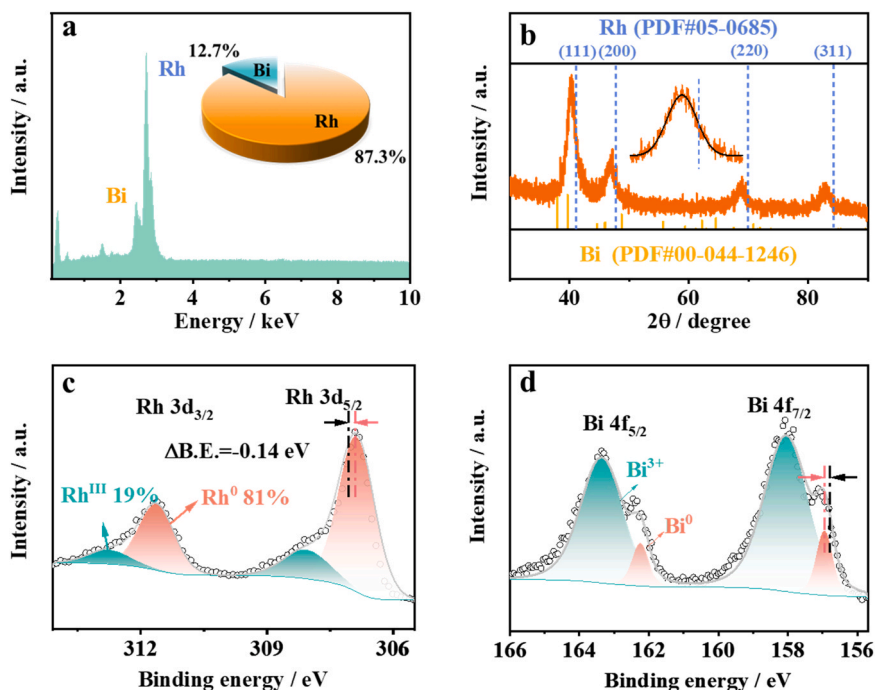


Fig. 1. (a) EDX pattern, (b) XRD pattern, (c) Rh 3d XPS spectrum, and (d) Bi 4f XPS spectrum of Rh₇Bi₁-NDs.

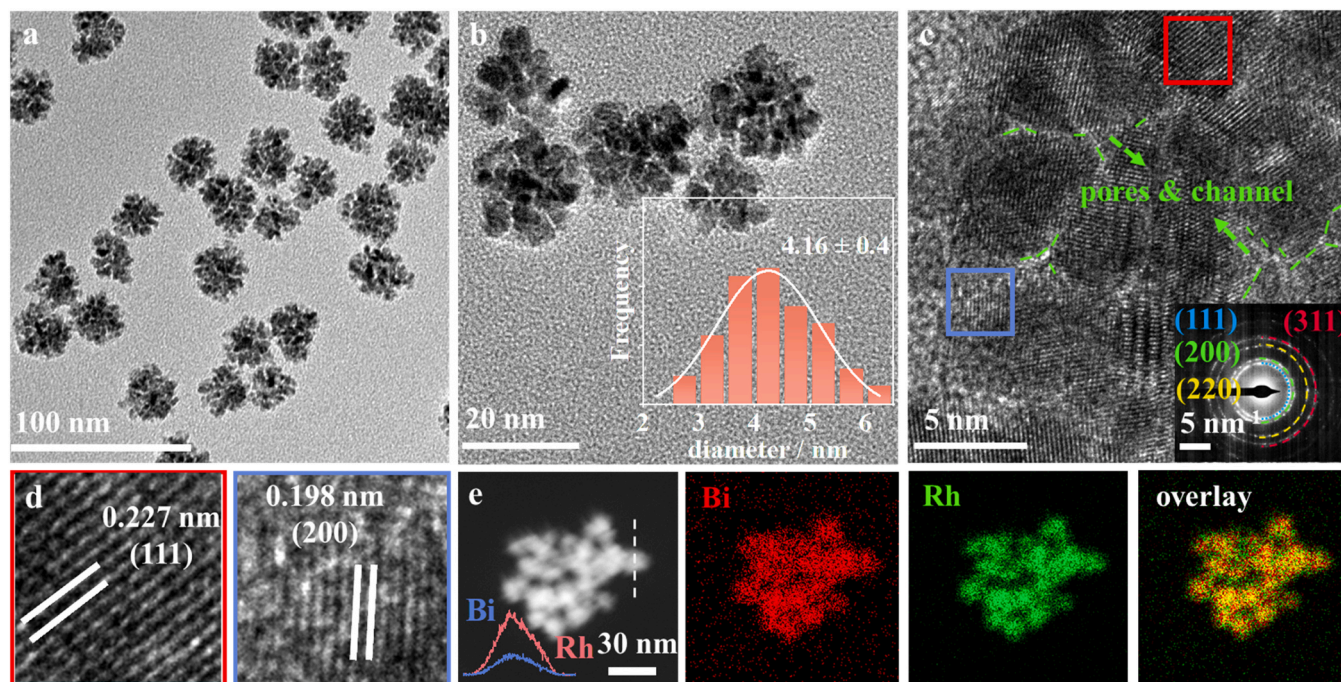


Fig. 2. (a–b) TEM image (insert: particle size distribution histogram), (c) HRTEM image and corresponding SAED pattern, (d) EDX mapping image, and (e) STEM image, line scanning profiles and elemental distribution images of Rh₇Bi₁-NDs.

respectively (Fig. 2d). The introduction of Bi results in a slight expansion of the Rh lattice, namely the strain effect, which can modify the electronic structure of Rh by adjusting its d-band structure and in turn affecting its adsorption behavior. Besides, the lattice expansion of Rh₇Bi₁-NDs also confirms the RhBi alloy structure [42]. EDX linear scanning and elemental distribution analysis of Rh₇Bi₁-NDs were performed by using scanning transmission electron microscopy (STEM). The characterization results indicate that Rh and Bi are uniformly

distributed in Rh₇Bi₁-NDs, further demonstrating the alloy structure of Rh₇Bi₁-NDs (Fig. 2e). The above characterization confirms the successful preparation of Rh₇Bi₁-NDs with a RhBi alloy structure. Notably, the unique multibranched structure of Rh₇Bi₁-NDs can inhibit Ostwald ripening during the electrochemical process and in turn enhance their stability [43]. Meanwhile, NDs can provide rich pores and channels to accelerate the mass transfer in the electrocatalytic reaction and enhance the electrocatalytic activity. Therefore, Rh₇Bi₁-NDs will be a good

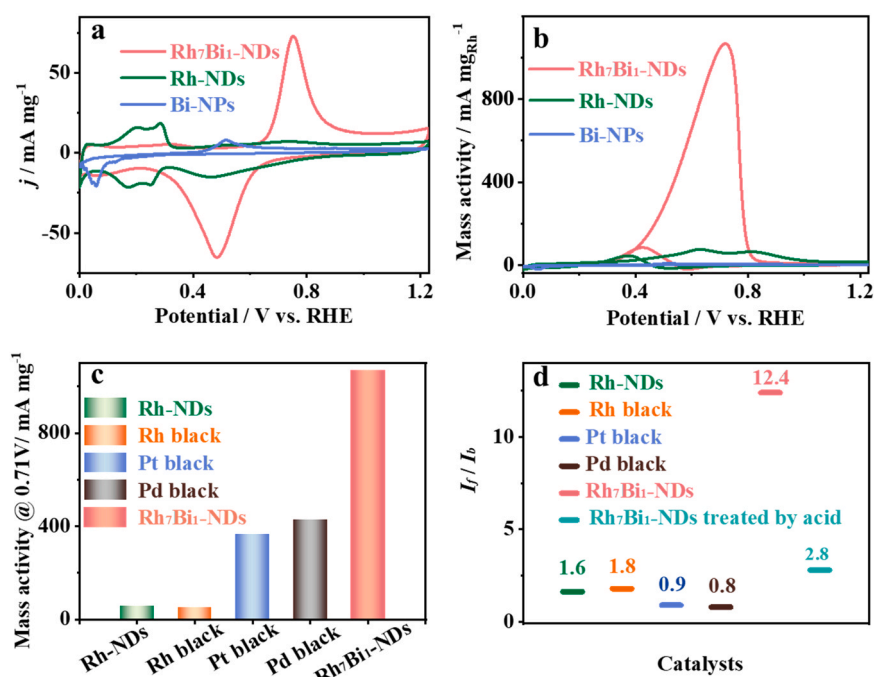


Fig. 3. (a) CV curves of Rh₇Bi₁-NDs, Rh-NDs and Bi NPs in nitrogen-saturated 1.0 M KOH electrolyte at 50 mV s⁻¹. (b) CV curves of Rh₇Bi₁-NDs, Rh-NDs and Bi NPs in nitrogen-saturated 1.0 M KOH electrolyte containing 0.5 M CH₃CH₂OH at 50 mV s⁻¹. (c) EOR mass activity of several catalysts at 0.71 V vs. RHE. (d) The I_f/I_b ratios of several catalysts derived from the EOR curves.

candidate for electrocatalyst.

2.2. EOR activity and anti-poisoning ability of Rh₇Bi₁-NDs

To effectively study the electrocatalytic performance of Rh₇Bi₁-NDs for EOR, Rh nanodendrites (Rh-NDs) and Bi nanoparticles (Bi-NPs) were synthesized for comparison (Fig. S2 and S3). The cyclic voltammetry (CV) curve of Rh₇Bi₁-NDs show a unique pair of redox peaks at 0.4–0.8 V, which is significantly different from the electrochemical properties of Rh-NDs and Bi-NPs (Fig. 3a). This pair of redox peaks is in the range of OH_{ad} adsorption and desorption. The special OH_{ad} adsorption and desorption behavior of Bi or Bi oxide on the surface of RhBi alloy can be attributed to the electronic interaction between Rh and Bi, which has also been found in other Bi-based alloy materials [44–47]. In addition, the typical hydrogen adsorption and desorption peaks of Rh are not found on Rh₇Bi₁-NDs, suggesting that the hydrogen adsorption is inhibited on the Rh₇Bi₁-NDs surface due to electron interactions in the RhBi alloy. The EOR activities of Rh₇Bi₁-NDs, Rh-NDs and Bi-NPs in alkaline electrolyte were investigated by the CV test. Compared to Bi-NPs without EOR activity and Rh-NDs with a poor EOR activity, Rh₇Bi₁-NDs exhibit significantly increased anodic current for the EOR (Fig. 3b). Considering that the adsorption behavior of hydrogen on Rh₇Bi₁-NDs surface is affected by the change of Rh electronic structure and interface environment, it is inaccurate to calculate electrochemically active surface area (ECSA) of Rh₇Bi₁-NDs by charge integral area of hydrogen adsorption and desorption region. So, ECSAs of Rh₇Bi₁-NDs and homemade Rh nanoparticles without NDs structure were tested using the copper underpotential deposition method (Fig. S4). The test results show that the ECSAs of Rh₇Bi₁-NDs and Rh nanoparticles are 21.51 and 15.05 m² g^{−1}, respectively. The high ECSA of Rh₇Bi₁-NDs is attributed to its unique three-dimensional NDs structure (Fig. S4). Their EOR activities were further normalized by ECSA, and the results show that Rh₇Bi₁-NDs exhibited significantly higher specific activity than Rh nanoparticles, indicating excellent inherent EOR activity of Rh₇Bi₁-NDs, in which the unique NDs structure provide rich pores and channels to accelerate the mass transfer during EOR (Fig. S4). Moreover, the mass activity of Rh₇Bi₁-NDs for the EOR is 1068.9 mA mg_{Rh}^{−1}, which is 14.3 times higher than that of Rh-NDs (74.3 mA mg_{Rh}^{−1}) and better than those of commercial Pt, Pd, and Rh catalysts (Fig. 3c, S5). Moreover, the mass activity of carbon-supported Rh₇Bi₁-NDs for the EOR can reach 2440 mA mg_{Rh}^{−1} (Fig. S6), which outperforms some advanced catalysts reported in recent years (Table 1). For the CV curve of EOR, the forward oxidation peak current (*I_f*) comes from direct ethanol oxidation, while the backward peak current (*I_b*) is usually attributed to the oxidation of some intermediates, such as CH_x or CO_{ad} [48–50]. Generally, higher *I_b* value indicates more severe poisoning. The *I_f*/*I_b* values of Rh-NDs and Rh₇Bi₁-NDs are 1.6 and 12.4, respectively, indicating that Rh₇Bi₁-NDs have enhanced catalytic oxidation activity for EOR intermediates and good anti-poisoning ability (Fig. 3d). Obviously, the introduction of the oxyphilic Bi metal can greatly increase the OH_{ad} adsorption at lower anodic potential compared to Rh. According to the so-called bifunctional mechanism, a large amount adsorbed OH_{ad} can facilitate the rapid removal of EOR intermediates on active Rh atoms adjacent to Bi atoms, resulting in the improved reactivity of Rh₇Bi₁-NDs [45,47,51–53]. To prove this, acid-treated Rh₇Bi₁-NDs was prepared, and the metallic Bi and oxidized state of Bi on the surface layer of Rh₇Bi₁-NDs can be effectively removed, as confirmed by XPS analysis (Fig. S7a). The CV test shows that the EOR activity of acid-treated Rh₇Bi₁-NDs is slightly lower than that of Rh₇Bi₁-NDs, but their *I_f*/*I_b* value is significantly decreased to 2.8 (Fig. S7b). This result demonstrates the shortage of OH_{ad} supply caused by the decrease of Bi component on the surface Rh₇Bi₁-NDs weakens the anti-poisoning ability. So, it can be further concluded that the bifunctional mechanism induced by Bi atoms on the Rh₇Bi₁-NDs surface is indeed conducive to improving EOR activity and anti-poisoning performance of Rh₇Bi₁-NDs. Meanwhile, the alloy structure of Rh₇Bi₁-NDs

Table 1

A summary of the EOR activity on noble metal-based electrocatalysts in alkaline electrolyte.

Catalyst	Electrolyte	Mass activity A mg _{Rh/Pt} ^{−1} at 0.71 V	Peak potential V vs. RHE	Year (Ref.)
RhBi-nanodendrites/ C	1 M KOH + 0.5 M CH ₃ CH ₂ OH	1.79	0.71	This work
RhBi-nanodendrites/ C	1 M KOH + 1 M CH ₃ CH ₂ OH	2.44	0.71	This work
C, S, N-polymer-Pd	1 M KOH + 1 M CH ₃ CH ₂ OH	0.95	0.77	2023 [54]
Pd Sb rhombohedra/ C	0.5 M NaOH + 0.5 M CH ₃ CH ₂ OH	1.78	0.93	2022 [44]
twin boundary-Pd/C	1 M KOH + 1 M CH ₃ CH ₂ OH	1.50	0.77	2022 [55]
Pd ₅₀ Bi ₁ nanowires	1 M KOH + 1 M CH ₃ CH ₂ OH	2.40	0.88	2021 [46]
0.2SnO ₂ -Rh nanosheets/C	0.1 M KOH + 0.5 M CH ₃ CH ₂ OH	0.19	0.78	2021 [38]
Pd/ graphene-Ni ₃ N	1 M NaOH + 1 M CH ₃ CH ₂ OH	2.10	0.87	2021 [56]
Au@Pt-Pd hemispherical nanostructures	1 M KOH + 1 M CH ₃ CH ₂ OH	1.60	0.88	2021 [57]
Holey Pt nanotubes	1 M KOH + 1 M CH ₃ CH ₂ OH	1.00	0.80	2021 [58]
Pd/Ni-P Nanoplates	1 M KOH + 1 M CH ₃ CH ₂ OH	2.00	0.79	2020 [59]

can also modify the catalytic behavior of Rh for the EOR through bimetallic effect, seems to be more critical to the enhancement of EOR activity on Rh.

2.3. EOR activity, selectivity and stability of RhBi-NDs

Subsequently, two other RhBi-NDs with different compositions, including Rh₅Bi₁-NDs and Rh₁₀Bi₁-NDs, were prepared to further investigate the effect of Bi content in RhBi-NDs on their EOR activity (Fig. S8). CV curves show that Rh₇Bi₁-NDs have the largest oxidation peak current, indicating an optimal EOR activity among these RhBi-NDs (Fig. 4a). Then, the Tafel lines are calculated with the slope fitted to be 125, 98 and 116 mV dec^{−1} for Rh₁₀Bi₁-NDs, Rh₇Bi₁-NDs and Rh₅Bi₁-NDs, respectively, implying rapidest EOR kinetics on Rh₇Bi₁-NDs (Fig. 4b). Manily, the Bi content in Rh₇Bi₁-NDs is optimized, which balances the effective regulation of Rh electronic structure and the exposure of Rh active sites. The EOR products on these catalysts were further investigated to disclose the role of Bi in the EOR pathway of Rh-based materials. The results from the nuclear magnetic resonance hydrogen spectroscopy (¹H NMR) of the electrolyte show that only acetic acid is detected as a product of EOR on these Rh-based catalysts (Fig. S9). The concentration of acetic acid was measured by high performance liquid chromatography (HPLC), and the Faradaic efficiency of the C2 product was further calculated (Fig. 4c), which is 80.8% for Rh₁₀Bi₁-NDs, 68.9% for Rh₇Bi₁-NDs, 81.0% for Rh₅Bi₁-NDs, and 86.3% for Rh NDs. Accordingly, the Faradaic efficiency of the C1 product (F_{C1}) can be calculated as 19.2% for Rh₁₀Bi₁-NDs, 31.1% for Rh₇Bi₁-NDs, 19% for Rh₅Bi₁-NDs, and 13.3% for Rh-NDs (Fig. 4c). Undoubtedly, the introduction of Bi can evidently improve the selectivity of Rh to the C1 pathway of EOR, which leads to excellent EOR activity of RhBi-NDs. Notably, Rh₇Bi₁-NDs shows the highest F_{C1}, which in turn delivers the highest EOR activity. Furthermore, chronoamperometry tests are performed to test the long-term EOR stability of Rh₇Bi₁-NDs and other commercial catalysts, which is an important performance index of

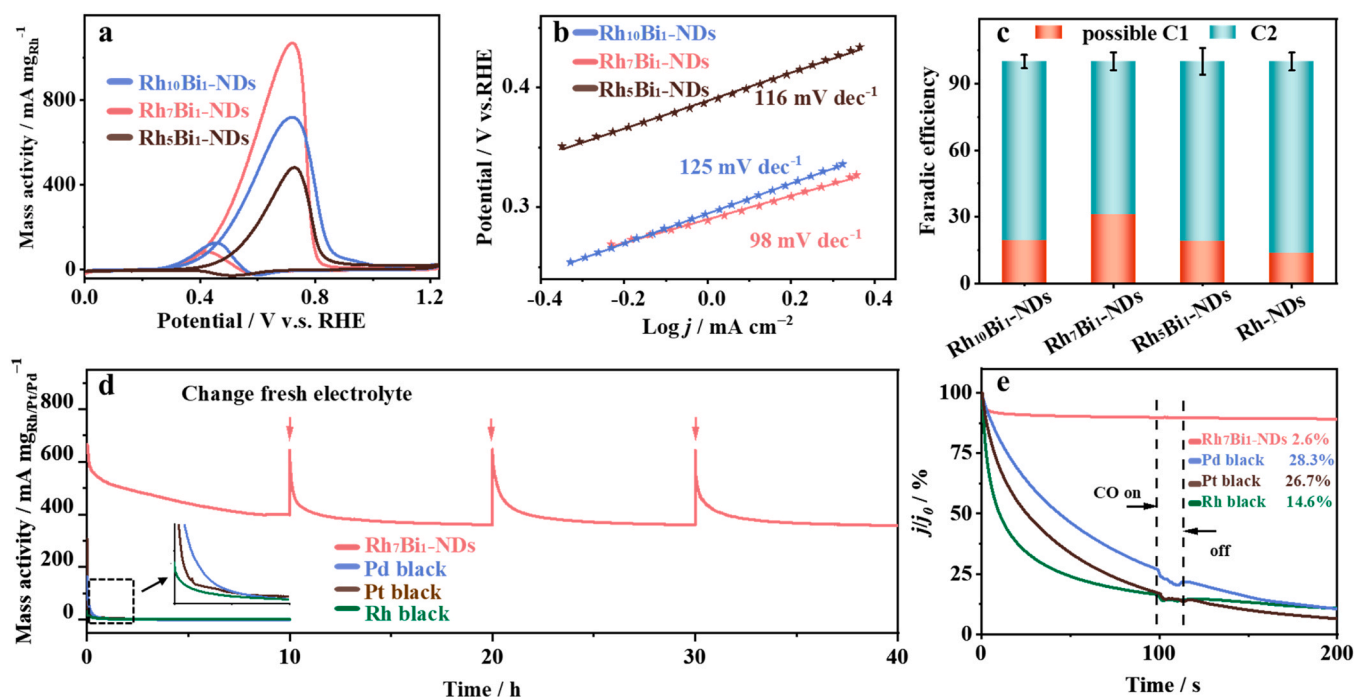


Fig. 4. (a) CV curves of several RhBi-NDs in nitrogen-saturated 1.0 M KOH electrolyte containing 0.5 M CH₃CH₂OH at 50 mV s⁻¹. (b) Tafel plots of EOR on several RhBi-NDs. (c) The Faradaic efficiency of EOR products on several RhBi-NDs. (d) Chronoamperometry curve of several RhBi-NDs at 0.62 V in nitrogen-saturated 1.0 M KOH with 0.5 M ethanol. (e) The chronoamperometric curves of several catalysts at 0.62 V after the introduction of CO.

catalysts in practical application. Compared to commercial Pt black, Pd black and Rh black, Rh₇Bi-NDs exhibit the lowest current decay and maintains the highest mass activity during the stability test (Fig. 4d). More impressively, the outstanding mass activity of Rh₇Bi-NDs can be easily recovered by using fresh electrolyte, allowing continuous operation for 40 h without obvious deactivation. After the stability test, the dendritic morphology of Rh₇Bi-NDs is still maintained, indicating that Rh₇Bi-NDs have a good structural stability. In addition, the EDX spectra show no significant changes in the chemical composition of Rh₇Bi-NDs before and after the stability test, indicating a high stability of the elemental composition. This good structural and composition stability of Rh₇Bi-NDs can be due to the uniform alloying of RhBi and the corrosion resistant three-dimensional dendritic structure (Fig. S10). Concurrently, the EOR stabilities of other RhBi-NDs are also much better than that of commercial Rh black, which is probably related to the improved anti-poisoning ability of Rh due to the introduction of oxyphilic Bi (Fig. S11). To further investigate the excellent stability of Rh₇Bi-NDs, CO was introduced into the electrolyte as a toxic reagent to study the performance degradation of these catalysts in stability tests. During test, the EOR current on Rh₇Bi-NDs decays by 2.6% after the introduction of CO, respectively, which are much lower than those on Pt black (26.7%), Pd black (28.3%) and Rh black (14.6%), demonstrating the enhanced anti-poisoning ability of RhBi-NDs as EOR electrocatalysts (Fig. 4e). According to bifunctional mechanisms, the oxyphilic Bi atoms on the surface of RhBi-NDs can provide abundant OH_{ad}, which play an important role in the oxidation of EOR intermediates formed by the C1 pathway, such as CH_x and CO, endowing RhBi-NDs with outstanding anti-poisoning ability and in turn significantly improved EOR stability. Compared with the easily poisoned commercial Pt black and Pd black, the CO stripping experiment results shows that Pt black and Pd black have obvious CO oxidation peaks (Fig. S12). In contrast the oxidation peak of Rh₇Bi-NDs almost overlapped with the OH_{ad} desorption peak, indicating weak CO adsorption which perhaps due to the large amount of OH_{ad} adsorption on the catalyst surface during its CO adsorption process. Obviously, the weak CO adsorption on the Rh₇Bi-NDs surface also contributes a weak poison effect and enhanced EOR stability.

2.4. EOR activity enhancement mechanism of Rh₇Bi-NDs

To investigate the enhancement mechanism of RhBi-NDs for EOR, theoretical calculations were performed for Rh(111) and RhBi(111) surfaces (Fig. S13). First, the d-band density of states (d-DOS) of Rh for Rh(111) and RhBi(111) surfaces was calculated. The results show that the d-band center of Rh in the RhBi(111) surface is -1.90 eV, which is closer to the Fermi level than that in the Rh(111) surface (-1.99 eV), suggesting that Bi can modify the electronic structure of Rh (Fig. 5a). Generally, a higher d-band center usually corresponds to a stronger binding strength of adsorbates on the Rh active site, which in turn cause the RhBi(111) surface to exhibit a different catalytic behavior from the Rh(111) surface for EOR. Then, to obtain free-energy diagram for EOR on Rh(111) and RhBi(111) surfaces, the Rh active site with the lowest adsorption energy was selected to calculate the Gibbs free energy change (ΔG) of each step (Fig. 5b).

The calculation results indicate that $\Delta G_{\text{CH}_3\text{CH}_2\text{OH}^*}$ is -1.37 eV and -1.65 eV on Rh(111) and RhBi(111) surfaces, respectively. Therefore, CH₃CH₂OH is more easily adsorbed and activated by the RhBi(111) surface, which is beneficial to the progress of the entire reaction. Under the ideal condition of U = 0 V, the step with the largest curve rise is the dehydrogenation and oxidation of CH₃CO* to CH₂CO*, which is the rate-determining step of the C1 pathway for EOR on both Rh(111) and RhBi(111) surfaces, consistent with the calculated results in the literature [60,61]. The energy barrier of the rate-determining step on the Rh(111) surface is 0.85 eV bigger than that on the RhBi(111) surface (0.78 eV), suggesting lower energy requirements on the RhBi(111) surface. Concurrently, the oxidation step of CH₃CO* to CH₃COOH* is exothermic on the Rh(111) surface but endothermic on the RhBi(111) surface, revealing that the C2 pathway of EOR is hindered on the RhBi(111) surface with respect to the Rh(111) surface. To obtain a more intuitive result about the rate-determining step, an extra voltage of 0.78 V is applied. In this case, the rate-determining step of C1 pathway is still endothermic reaction on the Rh(111) surface, requiring additional energy. On the contrary, the whole C1 pathway on the RhBi(111) surface shows a gentle downhill trend, and the ideal equilibrium state is

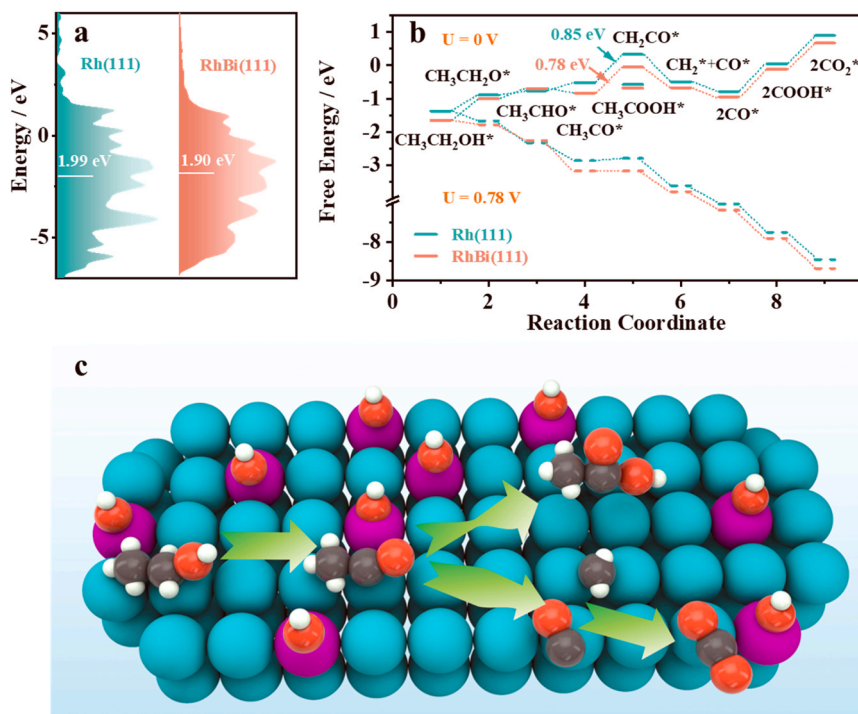


Fig. 5. (a) DOS plots of Rh for Rh(111) and RhBi(111) surfaces (d-band center is marked by a short solid line). (b) Free-energy diagram for EOR-related adsorption on Rh(111) and RhBi(111) surfaces at $U = 0/0.78$ V. (c) Schematic illustration of the mechanism for EOR on the RhBi(111) surface.

achieved at the rate-determining step without additional energy intake. The above theoretical calculation results indicate that enhanced CH₃CH₂OH adsorption, hindered C2 pathway and promoted C1 pathway support that RhBi alloy has better catalytic performance than Rh for EOR, which explains that RhBi-NDs exhibit significantly improved EOR activity and C1 product selectivity (Fig. 5c).

3. Conclusion

In summary, RhBi-NDs with the unique multibranch structure and rich pores/channels are prepared via a facile solvothermal method. Rh₇Bi₁-NDs with an optimal composition exhibit outstanding EOR activity (1068.9 mA mg⁻¹_{Rh}), outperforming other RhBi-NDs and commercial Pt, Pd, and Rh catalysts. ¹H NMR and HPLC experiments confirm that Rh₇Bi₁-NDs display a high F_{C1} of up to 31.1%. Concurrently, Rh₇Bi₁-NDs also reveal good electrocatalytic stability and excellent anti-poisoning ability for EOR due to the oxyphilic Bi atoms that provide abundant OH_{ad} for the oxidation of EOR intermediates. DFT calculations find that Bi in RhBi-NDs regulates the electronic structure of Rh, which promotes the C1 pathway of EOR on Rh active sites, leading to enhanced EOR performance. This work offers a design strategy for the structure and composition of Rh-based nanomaterials to achieve ethanol complete electrooxidation, providing some perspectives on the development of highly efficient and anti-poisoning non-Pt/Pd-based anode catalysts.

CRediT authorship contribution statement

Bo-Qiang Miao: Writing – original draft, Validation, Formal analysis, Visualization, Software, Methodology. **Bin Sun:** Validation, Formal analysis, Software, Methodology. **Tian-Jiao Wang:** Formal analysis, Software. **Feng Shi:** Formal analysis, Validation. **Pei Chen:** Formal analysis, Resources. **Pu-Jun Jin:** Formal analysis, Validation. **Dong-Sheng Li:** Software, Validation. **Fu-Min Li:** Methodology, Writing – review & editing, Funding acquisition, Resources. **Yu Chen:** Methodology, Writing – review & editing, Funding acquisition, Resources.

Declaration of Competing Interest

We declare that we have no financial and personal relationships with other people or organizations that can inappropriately influence our work, there is no professional or other personal interest of any nature or kind in any product, service and/or company that could be construed as influencing the position presented in, or the review of, the manuscript entitled.

Data availability

No data was used for the research described in the article.

Acknowledgements

This research was supported by the National Natural Science Foundation of China (22202076 and 22272103), the China postdoctoral science foundation (2022M711231), the Science and Technology Innovation Team of Shaanxi Province (2023-CX-TD-27 and 2022TD-35), the Fundamental Research Funds for the Central Universities (GK202202001 and GK202101005), and the 111 Project (B14041 and D20015).

Appendix A. Supporting information

Supplementary data associated with this article can be found in the online version at [doi:10.1016/j.apcatb.2023.122967](https://doi.org/10.1016/j.apcatb.2023.122967).

References

- [1] Q. Wang, S.J. Qing, Z. Gao, X.L. Tong, N.J. Yang, Modulating electronic structure of an Au-nanorod-core-PdPt-alloy-shell catalyst for efficient alcohol electro-oxidation, *Adv. Energy Mater.* 11 (2021) 2100812, <https://doi.org/10.1002/aenm.202100812>.
- [2] Y. Qiu, J. Zhang, J. Jin, J. Sun, H. Tang, Q. Chen, Z. Zhang, W. Sun, G. Meng, Q. Xu, Y. Zhu, A. Han, L. Gu, D. Wang, Y. Li, Construction of Pd-Zn dual sites to enhance the performance for ethanol electro-oxidation reaction, *Nat. Commun.* 12 (2021) 5273, <https://doi.org/10.1038/s41467-021-25600-9>.

- [3] Y. Sun, S. Polani, F. Luo, S. Ott, P. Strasser, F. Dionigi, Advancements in cathode catalyst and cathode layer design for proton exchange membrane fuel cells, *Nat. Commun.* 12 (2021) 5984, <https://doi.org/10.1038/s41467-021-25911-x>.
- [4] Z.P. Cano, D. Banham, S.Y. Ye, A. Hintennach, J. Lu, M. Fowler, Z.W. Chen, Batteries and fuel cells for emerging electric vehicle markets, *Nat. Energy* 3 (2018) 279–289, <https://doi.org/10.1038/s41560-018-0108-1>.
- [5] Y.N. Li, Q.L. Hong, B.Q. Miao, T.J. Wang, Y. Ding, Y. Chen, Platinum-tellurium alloy metallene toward formic acid oxidation reaction, *Renewables* 1 (2023) 90–99, <https://doi.org/10.31635/renewables.022.202200005>.
- [6] T.J. Wang, Y.C. Jiang, J.W. He, F.M. Li, Y. Ding, P. Chen, Y. Chen, Porous palladium phosphide nanotubes for formic acid electrooxidation, *Carbon Energy* 4 (2022) 283–293, <https://doi.org/10.1002/cey2.170>.
- [7] H. Tabassum, R. Zou, G. Wu, High-entropy nanomaterials for electrochemical energy conversion and storage, *Energy Lab* 1 (2023) 1, <https://doi.org/10.54227/elab.20220006>.
- [8] H. Adabi, A. Shakouri, N.U. Hassan, J.R. Varcoc, B. Zulevi, A. Serov, J. R. Regalbuto, W.E. Mustain, High-performing commercial Fe–N–C cathode electrocatalyst for anion-exchange membrane fuel cells, *Nat. Energy* 6 (2021) 834–843, <https://doi.org/10.1038/s41560-021-00878-7>.
- [9] W. Zhang, Y. Yang, B. Huang, F. Lv, K. Wang, N. Li, M. Luo, Y. Chao, Y. Li, Y. Sun, Z. Xu, Y. Qin, W. Yang, J. Zhou, Y. Du, D. Su, S. Guo, Ultrathin PtNiM (M = Rh, Os, and Ir) nanowires as efficient fuel oxidation electrocatalytic materials, *Adv. Mater.* 31 (2019), e1805833, <https://doi.org/10.1002/adma.201805833>.
- [10] Y. Sun, H.Y. Xiang, H.M. Li, G. Yu, H. Chen, S. Liu, High stability three-dimensional porous PtSn nano-catalyst for ethanol electro-oxidation reaction, *Chin. Chem. Lett.* 31 (2020) 2491–2494, <https://doi.org/10.1016/j.ccl.2020.04.025>.
- [11] V. Baglio, Direct ethanol fuel cells fluorine-doping boosts performance, *Nat. Energy* 6 (2021) 1096–1097, <https://doi.org/10.1038/s41560-021-00955-x>.
- [12] Y.Y. Zhang, J.G. Wang, X.F. Yu, D.R. Baer, Y. Zhao, L.Q. Mao, F.Y. Wang, Z.H. Zhu, Potential-dynamic surface chemistry controls the electrocatalytic processes of ethanol oxidation on gold surfaces, *ACS Energy Lett.* 4 (2019) 215–221, <https://doi.org/10.1021/acscenergylett.8b02019>.
- [13] X.Y. Fu, C.Z. Wan, Y. Huang, X.F. Duan, Noble metal based electrocatalysts for alcohol oxidation reactions in alkaline media, *Adv. Funct. Mater.* 32 (2022) 2106401, <https://doi.org/10.1002/adfm.202106401>.
- [14] L. Hui, X. Zhang, Y. Xue, X. Chen, Y. Fang, C. Xing, Y. Liu, X. Zheng, Y. Du, C. Zhang, F. He, Y. Li, Highly dispersed platinum chlorine atoms anchored on gold quantum dots for a highly efficient electrocatalyst, *J. Am. Chem. Soc.* 144 (2022) 1921–1928, <https://doi.org/10.1021/jacs.1c12310>.
- [15] X. Zhou, Y. Ma, Y. Ge, S. Zhu, Y. Cui, B. Chen, L. Liao, Q. Yun, Z. He, H. Long, L. Li, B. Huang, Q. Luo, L. Zhai, X. Wang, L. Bai, G. Wang, Z. Guan, Y. Chen, C.S. Lee, J. Wang, C. Ling, M. Shao, Z. Fan, H. Zhang, Preparation of Au@Pd core-shell nanorods with fcc-2h-fcc heterophase for highly efficient electrocatalytic alcohol oxidation, *J. Am. Chem. Soc.* 144 (2022) 547–555, <https://doi.org/10.1021/jacs.1c11313>.
- [16] H.A. Firouzjaie, W.E. Mustain, Catalytic advantages, challenges, and priorities in alkaline membrane fuel cells, *ACS Catal.* 10 (2020) 225–234, <https://doi.org/10.1021/acscatal.9b03892>.
- [17] Y. Zhang, X. Liu, T. Liu, X. Ma, Y. Feng, B. Xu, W. Cai, Y. Li, D. Su, Q. Shao, X. Huang, Rhombohedral Pd-Sb nanoplates with pd-terminated surface: an efficient bifunctional fuel-cell catalyst, *Adv. Mater.* 34 (2022), e2202333, <https://doi.org/10.1002/adma.202202333>.
- [18] Y. Yu, S.J. You, J.N. Du, Z.P. Xing, Y. Dai, H. Chen, Z. Cai, N.Q. Ren, J.L. Zou, ZIF-67-derived CoO (tetrahedral Co²⁺)@nitrogen-doped porous carbon protected by oxygen vacancies-enriched SnO₂ as highly active catalyst for oxygen reduction and Pt co-catalyst for methanol oxidation, *Appl. Catal. B-Environ.* 259 (2019), 118043, <https://doi.org/10.1016/j.apcatb.2019.118043>.
- [19] L. Zhao, X.L. Sui, J.Z. Li, J.J. Zhang, L.M. Zhang, G.S. Huang, Z.B. Wang, Supramolecular assembly promoted synthesis of three-dimensional nitrogen doped graphene frameworks as efficient electrocatalyst for oxygen reduction reaction and methanol electrooxidation, *Appl. Catal. B-Environ.* 231 (2018) 224–233, <https://doi.org/10.1016/j.apcatb.2018.03.020>.
- [20] F. Guo, M. Zhang, S. Yi, X. Li, R. Xin, M. Yang, B. Liu, H. Chen, H. Li, Y. Liu, Metal-coordinated porous polydopamine nanospheres derived Fe₃N-FeCo encapsulated N-doped carbon as a highly efficient electrocatalyst for oxygen reduction reaction, *Nano Res. Energy* 1 (2022), e9120027, <https://doi.org/10.26599/nre.2022.9120027>.
- [21] Y. Xu, H. Xue, X. Li, X. Fan, P. Li, T. Zhang, K. Chang, T. Wang, J. He, Application of metal-organic frameworks, covalent organic frameworks and their derivatives for the metal-air batteries, *Nano Res. Energy* (2023), <https://doi.org/10.26599/nre.2023.9120052>.
- [22] J.S. Guo, R.R. Chen, F.H. Zhu, S.G. Sun, H.M. Villullas, New understandings of ethanol oxidation reaction mechanism on Pd/C and Pd₂Ru/C catalysts in alkaline direct ethanol fuel cells, *Appl. Catal. B-Environ.* 224 (2018) 602–611, <https://doi.org/10.1016/j.apcatb.2017.10.037>.
- [23] X. Yang, Z. Liang, S. Chen, M. Ma, Q. Wang, X. Tong, Q. Zhang, J. Ye, L. Gu, N. Yang, A phosphorus-doped Ag@Pd catalyst for enhanced C–C bond cleavage during ethanol electrooxidation, *Small* 16 (2020), e2004727, <https://doi.org/10.1002/smll.202004727>.
- [24] Y.M. Zhu, L.Z. Bu, Q. Shao, X.Q. Huang, Structurally ordered Pt₃Sn nanofibers with highlighted antipoisoning property as efficient ethanol oxidation electrocatalysts, *ACS Catal.* 10 (2020) 3455–3461, <https://doi.org/10.1021/acscatal.9b04313>.
- [25] Y. Qin, H. Huang, W. Yu, H. Zhang, Z. Li, Z. Wang, J. Lai, L. Wang, S. Feng, Porous PdWM (M = Nb, Mo and Ta) trimetallene for high C1 selectivity in alkaline ethanol oxidation reaction, *Adv. Sci.* 9 (2022), e2103722, <https://doi.org/10.1002/advs.202103722>.
- [26] Z. Liang, L. Song, S. Deng, Y. Zhu, E. Stavitski, R.R. Adzic, J. Chen, J.X. Wang, Direct 12-electron oxidation of ethanol on a ternary Au(core)-PtIr(shell) electrocatalyst, *J. Am. Chem. Soc.* 141 (2019) 9629–9636, <https://doi.org/10.1021/jacs.9b03474>.
- [27] H.C. Peng, J. Ren, Y.C. Wang, Y. Xiong, Q.C. Wang, Q. Li, X. Zhao, L.S. Zhan, L. R. Zheng, Y.G. Tang, Y.P. Lei, One-stone, two birds: Alloying effect and surface defects induced by Pt on Cu₂-Se nanowires to boost C–C bond cleavage for electrocatalytic ethanol oxidation, *Nano Energy* 88 (2021), 106307, <https://doi.org/10.1016/j.nanoen.2021.106307>.
- [28] W. Chen, S. Luo, M. Sun, X. Wu, Y. Zhou, Y. Liao, M. Tang, X. Fan, B. Huang, Z. Quan, High-entropy intermetallic PtRhBiSnSb nanoplates for highly efficient alcohol oxidation electrocatalysis, *Adv. Mater.* 34 (2022), e2206276, <https://doi.org/10.1002/adma.202206276>.
- [29] S. Luo, L. Zhang, Y. Liao, L. Li, Q. Yang, X. Wu, X. Wu, D. He, C. He, W. Chen, Q. Wu, M. Li, E.J.M. Hensen, Z. Quan, A tensile-strained Pt-Rh single-atom alloy remarkably boosts ethanol oxidation, *Adv. Mater.* 33 (2021), e2008508, <https://doi.org/10.1002/adma.202008508>.
- [30] H. Tian, R. Zhu, P. Deng, J. Li, W. Huang, Q. Chen, Y.Q. Su, C. Jia, Z. Liu, Y. Shen, X. Tian, Ultrathin Pd₃Pt₁Rh_{0.1} nanorings with strong C–C bond breaking ability for the ethanol oxidation reaction, *Small* 18 (2022), e2203506, <https://doi.org/10.1002/smll.202203506>.
- [31] W. Zhu, J. Ke, S.B. Wang, J. Ren, H.H. Wang, Z.Y. Zhou, R. Si, Y.W. Zhang, C. H. Yan, Shaping single-crystalline trimetallic Pt-Pd-Rh nanocrystals toward high-efficiency C–C splitting of ethanol in conversion to CO₂, *ACS Catal.* 5 (2015) 1995–2008, DOI: 10.1021/cs5018419.
- [32] Q. Wang, R. Zhu, P. Deng, J. Li, W. Huang, Q. Chen, Y.-Q. Su, C. Jia, Z. Liu, Z. Kang, Y. Shen, X. Tian, Rhodium decorated stable platinum nickel nanowires for effective ethanol oxidation reaction, *Sci. China Mater.* 66 (2022) 679–685, <https://doi.org/10.1007/s40843-022-2150-y>.
- [33] Y.M. Zhu, L.Z. Bu, Q. Shao, X.Q. Huang, Subnanometer PtRh nanowire with alleviated poisoning effect and enhanced C–C bond cleavage for ethanol oxidation electrocatalysis, *ACS Catal.* 9 (2019) 6607–6612, <https://doi.org/10.1021/acscatal.9b01375>.
- [34] M. Zhou, J. Liu, C. Ling, Y. Ge, B. Chen, C. Tan, Z. Fan, J. Huang, J. Chen, Z. Liu, Z. Huang, J. Ge, H. Cheng, Y. Chen, L. Dai, P. Yin, X. Zhang, Q. Yun, J. Wang, H. Zhang, Synthesis of Pd₃Sn and PdCuSn nanorods with L1₂ phase for highly efficient electrocatalytic ethanol oxidation, *Adv. Mater.* 34 (2022), e2106115, <https://doi.org/10.1002/adma.202106115>.
- [35] F. Lv, W.Y. Zhang, M.Z. Sun, F.X. Lin, T. Wu, P. Zhou, W.X. Yang, P. Gao, B. L. Huang, S.J. Guo, Au clusters on Pd nanosheets selectively switch the pathway of ethanol electrooxidation: amorphous/crystalline interface matters, *Adv. Energy Mater.* 11 (2021) 2100187, <https://doi.org/10.1002/aenm.202100187>.
- [36] Y. Wang, M. Zheng, Y. Li, C. Ye, J. Chen, J. Ye, Q. Zhang, J. Li, Z. Zhou, X.Z. Fu, J. Wang, S.G. Sun, D. Wang, p-d orbital hybridization induced by a monodispersed ga site on a Pt₃Mn nanocatalyst boosts ethanol electrooxidation, *Angew. Chem. Int. Ed.* 61 (2022), e202115735, <https://doi.org/10.1002/anie.202115735>.
- [37] G. Liu, W. Zhou, Y. Ji, B. Chen, G. Fu, Q. Yun, S. Chen, Y. Lin, P.F. Yin, X. Cui, J. Liu, F. Meng, Q. Zhang, L. Song, L. Gu, H. Zhang, Hydrogen-intercalation-induced lattice expansion of Pd@Pt core-shell nanoparticles for highly efficient electrocatalytic alcohol oxidation, *J. Am. Chem. Soc.* 143 (2021) 11262–11270, <https://doi.org/10.1021/jacs.1c05856>.
- [38] S. Bai, Y. Xu, K. Cao, X. Huang, Selective ethanol oxidation reaction at the Rh-SnO₂ interface, *Adv. Mater.* 33 (2021), e2005767, <https://doi.org/10.1002/adma.202005767>.
- [39] Q.L. Hong, B.Q. Miao, T.J. Wang, F.M. Li, Y. Chen, Intermetallic PtTe metallene for formic acid oxidation assisted electrocatalytic nitrate reduction, *Energy Lab* 1 (2023), 220022, <https://doi.org/10.54227/elab.202200022>.
- [40] H. Wang, H. Zheng, L. Ling, Q. Fang, L. Jiao, L. Zheng, Y. Qin, Z. Luo, W. Gu, W. Song, C. Zhu, Pd metallene aerogels with single-atom W doping for selective ethanol oxidation, *ACS Nano* 16 (2022) 21266–21274, <https://doi.org/10.1021/acsnano.2c09270>.
- [41] W.L. Yan Qiao, Kai Huang, Tingting Yu, Qiyao Wang, Lei Gao, Zhilong Yang, Zesong Ma, Tulai Sun, Min Liu, Cheng Lian, Hongwen Huang, Engineering the local microenvironment over Bi nanosheets for highly selective electrocatalytic conversion of CO₂ to HCOOH in strong acid, *ACS Catal.* 12 (2022) 2357–2364, <https://doi.org/10.1021/acscatal.1c05135>.
- [42] F. Gao, Y. Zhang, H. You, Z. Li, B. Zou, Y. Du, Solvent-mediated shell dimension reconstruction of core@shell PdAu@Pd nanocrystals for robust C1 and C2 alcohol electrocatalysis, *Small* 17 (2021), e2101428, <https://doi.org/10.1002/smll.202101428>.
- [43] H. Liu, R.R. Jia, C.J. Qin, Q. Yang, Z.B. Tang, M.G. Li, Z.H. Ma, Anti-co poisoning FePtRh nanoflowers with Rh-rich core and Fe-rich shell boost methanol oxidation electrocatalysis, *Adv. Funct. Mater.* 33 (2022) 2210626, <https://doi.org/10.1002/adfm.202210626>.
- [44] B. Xu, T. Liu, X. Liang, W. Dou, H. Geng, Z. Yu, Y. Li, Y. Zhang, Q. Shao, J. Fan, X. Huang, Pd-Sb rhombohedra with an unconventional rhombohedral phase as a trifunctional electrocatalyst, *Adv. Mater.* 34 (2022), e2206528, <https://doi.org/10.1002/adma.202206528>.
- [45] S.M. Han, Y. Ma, Q.B. Yun, A.L. Wang, Q.S. Zhu, H. Zhang, C.H. He, J. Xia, X. M. Meng, L. Gao, W.B. Cao, Q.P. Lu, The synergy of tensile strain and ligand effect in PtBi nanorings for boosting electrocatalytic alcohol oxidation, *Adv. Funct. Mater.* 32 (2022) 2208760, <https://doi.org/10.1002/adfm.202208760>.
- [46] H.J. Wang, L. Jiao, L.R. Zheng, Q. Fang, Y. Qin, X. Luo, X.Q. Wei, L.Y. Hu, W.L. Gu, J. Wen, C.Z. Zhu, PdBi single-atom alloy aerogels for efficient ethanol oxidation, *Adv. Funct. Mater.* 31 (2021) 2103465, <https://doi.org/10.1002/adfm.202103465>.

- [47] M. Chu, J. Huang, J. Gong, Y. Qu, G. Chen, H. Yang, X. Wang, Q. Zhong, C. Deng, M. Cao, J. Chen, X. Yuan, Q. Zhang, Synergistic combination of Pd nanosheets and porous Bi(OH)₃ boosts activity and durability for ethanol oxidation reaction, *Nano Res.* 15 (2022) 3920–3926, <https://doi.org/10.1007/s12274-021-4049-9>.
- [48] M. Li, Z. Zhao, W. Zhang, M. Luo, L. Tao, Y. Sun, Z. Xia, Y. Chao, K. Yin, Q. Zhang, L. Gu, W. Yang, Y. Yu, G. Lu, S. Guo, Sub-monolayer YO_x/MoO_x on ultrathin Pt nanowires boosts alcohol oxidation electrocatalysis, *Adv. Mater.* 33 (2021), e2103762, <https://doi.org/10.1002/adma.202103762>.
- [49] K. Liu, W. Wang, P.H. Guo, J.Y. Ye, Y.Y. Wang, P.T. Li, Z.X. Lyu, Y.S. Geng, M. C. Liu, S.F. Xie, Replicating the defect structures on ultrathin Rh nanowires with Pt to achieve superior electrocatalytic activity toward ethanol oxidation, *Adv. Funct. Mater.* 29 (2019) 1806300, <https://doi.org/10.1002/adfm.201806300>.
- [50] C. Zhu, B. Lan, R. Wei, C. Wang, Y. Yang, Potential-dependent selectivity of ethanol complete oxidation on Rh electrode in alkaline media: a synergistic study of electrochemical ATR-SEIRAS and IRAS, *ACS Catal.* 9 (2019) 4046–4053, <https://doi.org/10.1021/acscatal.9b00138>.
- [51] B. Lan, Q. Wang, Z. Ma, Y. Wu, X. Jiang, W. Jia, C. Zhou, Y. Yang, Efficient electrochemical ethanol-to-CO₂ conversion at rhodium and bismuth hydroxide interfaces, *Appl. Catal. B-Environ.* 300 (2022), 120728, <https://doi.org/10.1016/j.apcatb.2021.120728>.
- [52] Y. Liu, B. Lan, Y. Yang, Boosting ethanol electrooxidation at RhBi alloy and Bi₂O₃ composite surfaces in alkaline media, *J. Mater. Chem. A* 10 (2022) 20946–20952, <https://doi.org/10.1039/d2ta06062k>.
- [53] H. Lv, L. Sun, Y. Wang, S. Liu, B. Liu, Highly curved, quasi-single-crystalline mesoporous metal nanoplates promote C-C bond cleavage in ethanol oxidation electrocatalysis, *Adv. Mater.* 34 (2022), e2203612, <https://doi.org/10.1002/adma.202203612>.
- [54] Z.H. You, Z.J. Zhao, Q.K. Zhang, C.H. Zhang, X.J. Long, D.H. Li, Y.Z. Xia, Organic heterocyclic strategy for precisely regulating electronic state of palladium interface to boost alcohol oxidation, *Adv. Funct. Mater.* 33 (2022) 2210877, <https://doi.org/10.1002/adfm.202210877>.
- [55] C. Liu, Y. Shen, J.F. Zhang, G. Li, X.R. Zheng, X.P. Han, L.Y. Xu, S.Z. Zhu, Y. A. Chen, Y.D. Deng, W.B. Hu, Multiple twin boundary-regulated metastable Pd for ethanol oxidation reaction, *Adv. Energy Mater.* 12 (2022) 2103505, <https://doi.org/10.1002/aenm.202103505>.
- [56] T. Wu, X. Wang, A.E. Emre, J.C. Fan, Y.L. Min, Q.J. Xu, S.G. Sun, Graphene-nickel nitride hybrids supporting palladium nanoparticles for enhanced ethanol electrooxidation, *J. Energy Chem.* 55 (2021) 48–54, <https://doi.org/10.1016/j.jechem.2020.06.056>.
- [57] W. Liang, Y. Wang, L. Zhao, W. Guo, D. Li, W. Qin, H. Wu, Y. Sun, L. Jiang, 3d anisotropic Au@Pt-Pd hemispherical nanostructures as efficient electrocatalysts for methanol ethanol and formic acid oxidation reaction, *Adv. Mater.* 33 (2021), e2100713, <https://doi.org/10.1002/adma.202100713>.
- [58] T.J. Wang, H.Y. Sun, Q. Xue, M.J. Zhong, F.M. Li, X. Tian, P. Chen, S.B. Yin, Y. Chen, Holey platinum nanotubes for ethanol electrochemical reforming in aqueous solution, *Sci. Bull.* 66 (2021) 2079–2089, <https://doi.org/10.1016/j.scib.2021.05.027>.
- [59] P.F. Yin, M. Zhou, J. Chen, C. Tan, G. Liu, Q. Ma, Q. Yun, X. Zhang, H. Cheng, Q. Lu, B. Chen, Y. Chen, Z. Zhang, J. Huang, D. Hu, J. Wang, Q. Liu, Z. Luo, Z. Liu, Y. Ge, X.J. Wu, X.W. Du, H. Zhang, Synthesis of palladium-based crystalline@amorphous core-shell nanoplates for highly efficient ethanol oxidation, *Adv. Mater.* 32 (2020), e2000482, <https://doi.org/10.1002/adma.202000482>.
- [60] N. Ye, P.C. Zhao, X.Y. Qi, W.C. Sheng, Z. Jiang, T. Fang, Ethanol electro-oxidation on the PdSn-TaN/C catalyst in alkaline media: making tan capable of splitting C-C bond, *Appl. Catal. B-Environ.* 314 (2022), 121473, <https://doi.org/10.1016/j.apcatb.2022.121473>.
- [61] G. Zhang, D. Cao, S. Guo, Y. Fang, Q. Wang, S. Cheng, W. Zuo, Z. Yang, P. Cui, Tuning the selective ethanol oxidation on tensile-trained Pt(110) surface by ir single atoms, *Small* 18 (2022), e2202587, <https://doi.org/10.1002/smll.202202587>.